Expansion of the laser ablation vapor plume into a background gas: Part A, Analysis

Sy-Bor Wen[a)], Xianglei Mao [a)] , Ralph Greif [b)], Richard E. Russo [a)]

Abstract

A study of the gas dynamics of the vapor plume generated during laser ablation was conducted including a counter-propagating internal shockwave. The density, pressure, and temperature distributions between the external shockwave front and the sample surface were determined by solving the integrated conservation equations of mass, momentum, and energy. The positions of the shockwaves and the contact surface (boundary that separates the compressed ambient gas and the vapor plume) were obtained when the incident laser energy that is transferred to the vapor plume and to the background gas, E, and the vaporized sample mass, M, are specified. The values for E and M were obtained from a comparison of the calculated trajectories of the external shockwave and the contact surface with experimental results for a copper sample under different laser fluences. Thus E and M, which are the two dominant parameters for laser ablation and which cannot be measured directly, can be determined. In addition, the internal shockwave propagation within the vapor plume was determined; the interaction of the internal shockwave with the sample may be one

of the mechanisms inducing liquid sample ejection during laser ablation.

---

a) Lawrence Berkeley National Laboratory, Berkeley, CA 94720

b) Department of Mechanical Engineering, University of California, Berkeley, California 94720

Keywords: Laser ablation, ambient gas, plasma shielding, shockwave, vortex ring

Introduction

Laser ablation is a viable method for chemical analysis, nanoparticle generation, micromachining and pulsed laser film deposition. Although empirically utilized for many years, the dynamics of laser ablation still are not well known. Knowledge of the density, pressure, and temperature distributions within the plasma during the expansion stage, laser energy conversion efficiency, and the total vaporized mass during laser ablation would be beneficial for defining experimental parameters for specific applications. Simulations have been presented to model the complex phenomena during laser ablation [1-4]. Simulations using molecular dynamics have the capability of including non-thermal equilibrium effects during ultrashort pulse laser ablation. However, since the number of molecules to be considered is very large for dense samples, it is difficult to perform simulations covering the entire ablation process due to computational limitations, especially for ablation in high ambient gas pressure. Hence, simulations with molecular dynamics (MD) and direct simulation by Monte Carlo (DSMC) tend to focus on laser ablation during the first several hundred picoseconds to few nanoseconds from the beginning of the laser pulse when the laser energy converts to thermal and kinetic energy of the vaporized sample. During this time scale, the absence of thermal equilibrium is important and continuum hypotheses may not be accurate. Direct numerical simulation (DNS) using governing continuum equations with appropriate boundary conditions both near the sample surface and adjacent to the background gas is another way to simulate the laser ablation process. The gas dynamics during laser ablation are quite complex, which include the propagation of shockwaves and the subsequent steep gradients within the high temperature plasma region. Very fine temporal and spatial resolution for a pure 3D simulation is required for obtaining the gas dynamics during laser ablation by the

DNS. Therefore, it is time consuming to perform a 3D simulation of the laser ablation process by DNS. Often spherically symmetric flow fields are assumed and certain shockwaves and/or expansion waves are neglected. The DNS with these assumptions provides good results in the trajectories of shockwaves and contact surface between the vapor plume and the compressed background gas. This approach (DNS), even though it is more time efficient compared to other methods (MD and DSMC), still requires hours to simulate from the beginning to a few microseconds after the laser pulse ablates a sample in atmospheric background gas pressure. A more time efficient method is used in the present work to determine the laser energy conversion ratio and the vaporized sample mass by iterative comparison of the simulated and experimental trajectories of the external shockwave and contact surface. The present method is to build an analytical model which is able to predict the main mechanisms during laser ablation. Predtechensky et al. [1] used the conservation laws to evaluate the terminal size of the vapor plume during laser ablation. Arnold et al.[2] also used this approach to calculate the trajectories of the contact surface between the compressed background gas and the high temperature vapor plume. To expand these studies and to improve the accuracy in the predicted trajectories of the external shockwave and the contact surface, the dynamics of the internal shockwave within the vapor plume and the reflection mechanisms of internal shockwaves are included in this work. In addition, physical properties are assumed to be linear functions of position in certain regions rather than uniform property conditions that were used in previous studies. Besides the trajectories of the external shockwave and the contact surface, our approach improves the accuracy of the prediction of the temperature and pressure fields within the thermally affected region due to laser heating. Such knowledge is important in studies for chemical analysis by spectral line emission and of particle generation processes; both are sensitive to the temperature evolution of the vapor plume.

Analysis

An integral method is used in the present study [1,2]; density, pressure, and temperature distributions are assumed and the resulting governing equations are solved to determine the trajectories of the shockwaves and contact surfaces. The ablation process is divided into four consecutive stages. For each stage, specific density, pressure, and temperature distributions are used based on physical arguments and/or experimental data. Comparisons of the predicted positions of the contact surface and the external shockwave front are made with experimental data from shadowgraphs and ICCD (intensified CCD) images [5]. From the present simulation, the trajectory of the internal shockwave which propagates back and forth between the contact surface and the sample surface is also determined. The internal shockwave is a necessity for satisfying the continuity conditions for pressure and velocity at the contact surface for a supersonically expanding vapor plume.

- Stage one: from the end of the laser pulse to the time when the internal shock wave reaches the sample surface (fig. 1a). During this stage, the density, pressure, and temperature distributions in the unshocked vapor plume are approximated by the free expansion relation proposed by Kelly et al. [6]. The density, pressure, and temperature are assumed to be uniform throughout the internal shockwave region, SWi, and external shockwave region, SWe. The velocity in the unshocked vapor plume, internal shockwave region, and external shockwave region are approximated by linear functions.

- Stage two: the time from when the internal shock wave reaches the sample surface

and is reflected to the time when the reflected internal shockwave again reaches the contact surface (fig. 1b).

- Stage three: the time from when the internal shock wave reaches the contact surface and is reflected to the time when this internal shock wave again reaches the sample surface (fig. 1c).

- Stage four: The internal shockwave is neglected at this stage because its strength is weak compared to the sound wave. Only the external shockwave and high temperature vapor plume exist during stage four. The physical properties within the vapor plume are assumed to be uniform because the size of the vapor plume only slightly increases during this stage (fig. 1d). However, density, pressure, and temperature distributions within the external shockwave region are assumed to be linear because the external shockwave continues to expand to a much larger distance compared to the vapor plume.

The sequence for the vapor plume expansion after the laser pulse can be expressed by recurring stages $1 \rightarrow 2 \rightarrow 3 \rightarrow 2 \rightarrow 3... \rightarrow 4$ when the heat transfer by conduction, diffusion, and radiation are neglected. This approach is a good approximation during the first few hundred of nanoseconds after the laser pulse, when most energy loss of the vapor plume comes from the work done by the vapor plume on the compressed background gas. The governing equations for each stage are given below and are integrated with respect to time using Euler's method.

Stage One

Stage one starts from the end of the laser pulse to the time when the internal shockwave arrives the sample surface.

For nanosecond and longer pulsed laser ablation, significant sample evaporation ends roughly at the end of the laser pulse (≈two times the full width at half maximum (FWHM) of the laser pulse in the present work) [7]; for femtosecond laser pulse durations, evaporation stops within one nanosecond after the laser pulse [8]. Hence, for this study with time scale larger than a few nanoseconds, it is adequate to assume that sample evaporation stops just after the end of the laser pulse; the density, pressure, and temperature distributions are well established within the vapor plume at these time. In addition, the expansion of the vapor plume with a background gas is similar to that in a vacuum in this stage [2]; the physical property distributions within the vapor plume (in this stage) are almost the same with or without background gas. Two simple models can be used to describe the distributions of these properties for ablation in a vacuum; the free expansion model [9] which neglects the initial velocity of the vapor plume at the end of the laser pulse and another simplified model which includes this velocity derived by Luk'yanchuk et al. [3]. These two models converge with increasing time as the initial plume velocity effect becomes less important. Results of the propagation of the vapor plume and the distributions of the physical properties within the vapor plume from Luk'yanchuk's model under spherically symmetric conditions and for ideal monatomic gas are listed below [3]. These results will be used with the conservation equations for this stage of the plume.

$$\left(\frac{R}{R_o}\right)^2 \equiv \Psi(t) = 1 + 2\frac{u_o}{R_o}t + \left[\left(\frac{u_o}{R_o}\right)^2 + \frac{16}{3}\frac{E}{MR_o^{\,2}}\right]t^2 \tag{1.1}$$

$$\rho(t) = \rho_o\left(1-\xi^2\right)^{3/2}\Psi(t)^{-3/2},\ \rho_o = \frac{8}{\pi^2}\frac{M}{R_o^{\,3}} \tag{1.2}$$

$$T(t) = T_o\left(1-\xi^2\right)\Psi(t)^{-1},\ \mathrm{T}_o = \frac{\mu}{\Re_p}\frac{16}{15}\frac{E}{M}, \tag{1.3}$$

where $\xi = r/R(t)$ is the Lagrangian coordinate ($0 \le \xi \le 1$) with $\xi = 0$ at the origin

of the spherical symmetric center, $R(t)$ is the radius of the expanding plume, which is so far unaffected by the background gas, u_0 is the initial velocity of the vapor plume, $\Re_p$ is the gas constant of the vapor, and μ is the atomic weight of the vapor

The total mass in the unshocked vapor plume behind the internal shockwave front, R_i, can be evaluated as

$$M_p = \int_0^{R_i} \rho_p 4\pi r^2 dr = 4\pi\rho_o \Psi(t)^{-3/2} R^3 F_1\left[\frac{R_i}{R}\right] \tag{1.4}$$

where $F_1[x] = \int_0^x \left[1 - y^2\right]^{3/2} y^2 dy$

From (1.1), the velocity of the vapor plume when expanding in a vacuum can be expressed as

$$\dot{R} = R_o d\left[\Psi(t)^{1/2}\right]/dt \equiv R_o \Phi(t), \tag{1.5}$$

where

$$\Phi(t) = d\left[\Psi(t)^{1/2}\right]/dt = \left\{1 + 2\frac{u_o}{R_o}t + \left[\left(\frac{u_o}{R_o}\right)^2 + \frac{16}{3}\frac{E}{MR_o^{\,2}}\right]t^2\right\}^{-1/2} \left\{\frac{u_o}{R_o} + \left[\left(\frac{u_o}{R_o}\right)^2 + \frac{16}{3}\frac{E}{MR_o^{\,2}}\right]t\right\}$$

Assuming a linear velocity distribution within this region, the kinetic energy in the vapor plume is

$$E_{pk} = \int_0^{R_i} \rho_p \frac{V_p^{\,2}}{2} 4\pi r^2 dr = 2\rho_o \Psi(t)^{-3/2} R_o^{\,2} \Phi(t)^2 \pi R^3 F_2\left[\frac{R_i}{R}\right] \tag{1.6}$$

where $F_2[x] = \int_0^x \left[1 - y^2\right]^{3/2} y^4 dy$

The thermal energy stored in the vapor plume also can be evaluated from the following integral:

$$E_{pt} = \frac{1}{\gamma_p - 1} 4\pi \int_0^{R_i} \rho_p \Re_p T_p r^2 dr = \frac{1}{\gamma_p - 1} 4\pi \rho_o \Re_p T_o \Psi(t)^{-5/2} R^3 F_3 \left[\frac{R_i}{R} \right] \qquad (1.7)$$

where $F_3[x] = \int_0^x \left[1 - x^2\right]^{5/2} x^2 dx$

In the internal shockwave region (cf. figure 1a), a first order approximation is that density and pressure are uniform. The velocity is approximated by a linear function in order to satisfy both the boundary velocities at the contact surface and just behind the internal shockwave. Pressure and density are approximated as uniform in the external shockwave region (cf. figure 1a and 2) since the size of this region is very small during stage one (cf. fig. 6). These values are obtained from the jump conditions behind the external shockwave. The integral forms of the conservation relations of mass, momentum, and energy in all three regions are listed below. Six equations with six jump conditions across the internal and the external shockwaves (cf. Appendix A) are used to determine the variables within the three regions. The integral form for mass, momentum, and energy in each region is listed in Appendix A.

- *Mass conservation in the vapor plume*

$$M = M_p + M_i, \qquad (1.8)$$

which is equal to $\rho_i = \frac{M - M_p}{4\pi \left(R_c^3 - R_i^3\right)/3}$ under the assumption of uniform ρ_i.

assumption

- *Mass conservation in the external shockwave region*

$$M_e = \frac{4\pi}{3} R_e^{\,3} \rho_g = \frac{4\pi}{3} \left(R_e^{\,3} - R_c^{\,3}\right) \rho_e \qquad (1.9)$$

- *Momentum conservation in the external shockwave region*

$$\frac{dP_e}{dt} = \pi R_c^{\,2} p_c - \pi R_e^{\,2} p_g + \int_{R_c}^{R_e} p 2\pi r dr$$
$$= \pi R_c^{\,2} p_c - \pi R_e^{\,2} p_g + 2\pi \left[\left(\frac{p_e - p_c}{R_e - R_c} \right) \frac{1}{3} \left(R_e^{\,3} - R_c^{\,3} \right) + \left(\frac{R_e p_c - R_c p_e}{R_e - R_c} \right) \frac{1}{2} \left(R_e^{\,2} - R_c^{\,2} \right) \right] \tag{1.10}$$

- *Energy conservation of the whole system*

$$E_p + E_i + E_e = E_{laser} + \frac{4\pi}{3} \frac{p_g}{\gamma_g - 1} R_e^{\,3} \tag{1.11}$$

with $E_p = E_{pk} + E_{pt}$, $E_i = E_{ik} + E_{it}$, and $E_e = E_{et} + E_{ek}$ (subscript *t*=thermal energy and *k*=kinetic energy)

In addition, the pressures on both sides of the contact surface are the same, i.e.

$$p_c = p_i \tag{1.12}$$

and equal to the pressure behind the external shockwave, i.e.

$$p_e = p_c \tag{1.13}$$

Eleven variables are determined in this stage: ρ_i, p_i, p_c, u_i, R_i, R_c, $\dot{R}_c$, ρ_e p_e, u_{e1}, and R_e, for the twelve relations (eq. 1.8-1.13 + six jump conditions). The above conditions result from the assumption that both density and pressure are uniform within the internal shockwave region (SWi, cf. figure 1a) and have the same value as that just behind the internal shockwave. In addition, we also require the pressure within the internal shockwave region to be the same as that at the contact surface. Therefore, with the mass conservation in the internal shockwave region, there are four equations available ($p_i = p_c$, $p_i = f_{p,Jump}(R_i, \dot{R}_i)$, $\rho_i = f_{\rho,Jump}(R_i, \dot{R}_i)$ and $\rho_i = \frac{M - M_p}{4\pi \left(R_c^3 - R_i^3 \right) / 3}$) to determine three variables, ρ_i, p_i and $\dot{R}_i$. In Arnold et al. [2], the density of the entire internal shockwave region was assumed to be equal to the density behind the internal shockwave front ($\rho_i = f_{\rho,Jump}(R_i, \dot{R}_i)$ and

$\rho_i = \dfrac{M - M_p}{4\pi\left(R_c^3 - R_i^3\right)/3}$) and Eq. (1.12) was neglected; which describes the relation between the pressure above and behind the internal shockwave. The pressure at the contact surface was used as the characteristically uniform pressure in the entire internal shockwave region, which is not necessarily equal to the pressure immediately behind the internal shockwave front. According to Arnold et al [2], this assumption generates reasonable results until the internal shockwave region becomes large compared to the size of the vapor plume. An ultra high internal shockwave velocity will be predicted especially when the internal shockwave approaches the sample surface. As a result, the velocity in the internal shockwave region will become so large that the kinetic energy of this region will be greater than the total energy of the entire system; a non-physical result. Therefore, the approximation for the distribution of variables should be modified when the internal shockwave approaches the sample surface. The pressure distribution is more uniform compared to the density distribution behind a strong shockwave [4], when the internal shockwave approaches the sample surface with increasingly high Mach number. Therefore, in determining ρ_i, p_i and $\dot{R}_i$ from Eqs.(1.8-13), it is better to assume that the pressure is uniform between the internal shockwave and the contact surface with a value equal to the pressure just behind the internal shockwave (A.11) rather than assume the density is uniform between the internal shockwave and the contact surface with a value equal to the pressure just behind the internal shockwave (A.10) as in Arnold's work. Therefore, we use (A.11) and omit (A.10) for the second step simulation when the size of the internal shockwave region is large. The transition between the first and second steps is chosen when the pressure at the contact surface is the same as that just after the internal shockwave front. One consideration might be to omit (A.10) at the beginning

of the simulation and use the same set of equations throughout this stage. However, our numerical results show that the internal shock region will become thinner during the simulation and disappear by this approach; another possible solution of the Euler equations when the flow field is treated as incompressible. However, this is not a valid solution for our situation because shockwaves do appear during laser ablation. To achieve relevant solutions, it is necessary to divide the simulation of this stage into two steps if uniform property distributions are used in the internal shockwave region. In the beginning, the density within the internal shockwave can be treated as being uniform with the same value as that just after the internal shockwave front. When the pressure at the contact surface becomes the same as that after the internal shockwave front, (A.11) is then used instead of (A.10) in the simulation.

Stage Two

Stage two starts when the internal shockwave strikes the sample surface and last until the internal shockwave again strikes the contact surface.

When the internal shockwave strikes the sample, a weak reflected shockwave is generated from the surface. The density, pressure, and temperature within the two regions of the vapor plume that are divided by the internal shockwave front (cf. fig. 1b) are assumed to be uniform as a first order approximation. The corresponding parameters, excluding density, are assumed to vary linearly with distance within the external shockwave region for consistency with the first stage. The density within the external shockwave region (cf. fig. 1b and 3) is approximated as uniform as in stage one. The velocities within all regions are again assumed as linear functions of distance (cf. fig. 3). From the integral forms of the conservation laws of mass, momentum, and energy in each region, with jump conditions after normal shockwaves, relations for determining the density, pressure, temperature, and velocity distributions in all

regions can be determined. The integral form of mass, momentum, and energy in each region along with the jump conditions for the internal and the external shockwaves are listed in Appendix A.

- *Mass conservation in the unshocked plume region*

$$M_p = M - M_i = M - \frac{4\pi}{3}\rho_i R_i^3 = \frac{4\pi}{3}\rho_p \left(R_c^3 - R_i^3\right) \tag{2.1}$$

- *Momentum conservation in the unshocked plume region*

$$\frac{dP_p}{dt} = \pi R_i^2 \left(p_i - p_c\right) + \pi R_i^2 \rho_i \left(u_i - \dot{R}_i\right) u_i \tag{2.2}$$

- *Energy conservation in the unshocked plume region*

$$\frac{dE_p}{dt} = -\left(\frac{p_p}{\gamma_p - 1} + \frac{1}{2}\rho_p u_p^2\right)\left(\dot{R}_i - u_p\right)4\pi R_i^2 + p_c u_p 4\pi R_i^2 - p_c \dot{R}_c 4\pi R_c^2 \tag{2.2}$$

with $E_p = E_v - E_i = E_{pk} + E_{pt}$

- *Mass conservation in the internal shockwave region*

$$dM_i / dt = \rho_p \left(\dot{R}_i - u_p\right)4\pi R_i^2 \tag{2.4}$$

- *Energy conservation in the internal shockwave region*

$$\frac{dE_i}{dt} = \left(\frac{p_p}{\gamma_p - 1} + \frac{1}{2}\rho_p u_p^2\right)\left(\dot{R}_i - u_p\right)4\pi R_i^2 - p_c u_p 4\pi R_i^2, \text{ with } E_i = E_{ik} + E_{it} \tag{2.5}$$

- *Mass conservation in the external shockwave region*

$$M_e = \frac{4\pi}{3} R_e^3 \rho_g = \rho_e \frac{4\pi}{3}\left(R_e^3 - R_c^3\right) \tag{2.6}$$

- *Momentum conservation in the external shockwave region*

$$\frac{dP_e}{dt} = \pi R_c^{\,2} p_c - \pi R_e^{\,2} p_g + \int_{R_c}^{R_e} p 2\pi r dr$$
$$= \pi R_c^{\,2} p_c - \pi R_e^{\,2} p_g + 2\pi \left[\left(\frac{p_e - p_c}{R_e - R_c} \right) \frac{1}{3} \left(R_e^{\,3} - R_c^{\,3} \right) + \left(\frac{R_e p_c - R_c p_e}{R_e - R_c} \right) \frac{1}{2} \left(R_e^{\,2} - R_c^{\,2} \right) \right] \tag{2.7}$$

- *Energy conservation in the external shockwave region*

$$E_e = E_{laser} + \frac{4\pi}{3} \frac{p_g}{\gamma_g - 1} R_e^{\,3} - E_v, \text{ with } E_e = E_{et} + E_{ek} \tag{2.8}$$

Stage Three

Stage three begins when the reflected wave is generated at the contact surface and continues until this wave strikes the sample surface.

When the internal shockwave strikes the contact surface, a reflected wave is generated again and travels back toward the sample surface. The reflected wave can be either a shockwave or a rarefaction wave depending upon the relative magnitudes of the generalized acoustic impedance in the two adjoining media [10]. The temperature in the vapor plume is much higher than that of the external shockwave region; the density of the vapor plume must be much lower than that of the external shockwave region at least in the area near the contact surface. Hence, the effect when the internal shockwave strikes the contact surface will be similar to that when the internal shockwave strikes a solid layer, and the reflected wave should be a shockwave rather than a rarefaction wave.

Density, pressure, and temperature in the two regions of the vapor plume that are separated by the internal shockwave (cf. fig. 1c and 4) are assumed to be uniform as in the previous two stages. Velocities, as in every stage of this model, are assumed to have linear distributions satisfying jump conditions across shockwaves and the

continuous velocity requirement at the contact surface. The pressure within the internal shockwave region is taken to be uniform and equal to the value just after the internal shockwave, which can be evaluated from the jump conditions across a normal shockwave. However, the density within the internal shockwave region is not assumed to be equal to the density just after the internal shockwave as was discussed in the second stage section. Instead, an average density evaluated from the mass conservation relation is used as the characteristic density in the internal shockwave region. In contrast to the previous two stages, an additional refracted shockwave propagating inside the original external shockwave region now appears in this stage after the internal shockwave strikes the contact surface (cf. fig. 4). The integrated conservation laws in each region with jump conditions across the shockwaves are again used to determine the variables in this stage. The integral form of mass, momentum, and energy in each region along with the jump conditions for the internal and the external shockwaves are listed in Appendix A.

- *Mass conservation in the unshocked vapor plume region*

$$\frac{dM_p}{dt} = -4\pi R_i^2 \rho_p \left(u_p - \dot{R}_i\right), \text{ with } M_p = M - M_i = M - \frac{4\pi}{3}\rho_i \left(R_c^3 - R_i^3\right) = \frac{4\pi}{3}\rho_p R_i^3 \tag{3.1}$$

- *Energy conservation in the unshocked vapor plume region*

$$\frac{dE_p}{dt} = -4\pi\rho_p R_i^2 \left(u_p - \dot{R}_i\right)\left[\frac{\gamma_p}{\gamma_p - 1} R_p T_p + \frac{1}{2} u_p^2\right], \text{ with } E_p = E_{pk} + E_{pt} \tag{3.2}$$

- *Entropy conservation in the unshocked vapor plume region*

$$p_p = C_s \rho_p^{\gamma_p}, \text{ with } C_s = p_{p,end\ of\ stage2} / (\rho_{p,end\ of\ stage2})^{\gamma_p} \tag{3.3}$$

- *Mass conservation in the internal shockwave region*

$$M_i = \frac{4\pi}{3}\rho_i\left(R_c^{\,3} - R_i^{\,3}\right) \tag{3.4}$$

- *Energy conservation in the internal shockwave region*

$$\frac{dE_i}{dt} = -4\pi p_c R_c^{\,2}\dot{R}_c + 4\pi\rho_p R_i^{\,2}\left(u_p - \dot{R}_i\right)\left[\frac{\gamma_p}{\gamma_p - 1}R_p T_p + \frac{1}{2}u_p^{\,2}\right], \text{ with } \quad E_i = E_{ik} + E_{it} \tag{3.5}$$

- *Mass conservation in the external shockwave region*

$$\frac{dM_e}{dt} = 4\pi R_e^{\,2}\dot{R}_e\rho_g\,; \quad M_e = M_{e1} + M_{e2} \tag{3.6}$$

- *Momentum conservation in the external shockwave region*

$$\begin{aligned}\frac{dP_e}{dt} &= \pi R_c^{\,2}p_c - \pi R_e^{\,2}p_g + \int_{R_c}^{R_{e'}} p2\pi r dr + \int_{R_{e'}}^{R_e} p2\pi r dr \\ &= \pi R_c^{\,2}p_c - \pi R_e^{\,2}p_g + 2\pi\left[\left(\frac{p_{e2'} - p_c}{R_{e'} - R_c}\right)\frac{1}{3}\left(R_{e'}^{\,3} - R_c^{\,3}\right) + \left(\frac{R_{e'}p_c - R_c p_{e2'}}{R_{e'} - R_c}\right)\frac{1}{2}\left(R_{e'}^{\,2} - R_c^{\,2}\right)\right] \\ &+2\pi\left[\left(\frac{p_{e1} - p_{e1'}}{R_e - R_{e'}}\right)\frac{1}{3}\left(R_{e'}^{\,3} - R_c^{\,3}\right) + \left(\frac{R_e p_{e1'} - R_{e'}p_{e1}}{R_e - R_{e'}}\right)\frac{1}{2}\left(R_{e'}^{\,2} - R_c^{\,2}\right)\right]\end{aligned} \tag{3.7}$$

- *Energy conservation in the external shockwave region 1*

$$\frac{dE_1}{dt} = 4\pi R_e^{\,2}\dot{R}_e\frac{p_g}{\gamma_g - 1} - \left[4\pi R_{e'}^{\,2}\left(\dot{R}_{e'} - u_{e1'}\right)\frac{\gamma_g p_g}{\gamma_g - 1} + \frac{1}{2}\rho_{e1'}u_{e1'}^{\,2}\right], \text{ with } \quad E_{e1} = E_{e1t} + E_{e1k} \tag{3.8}$$

- *Energy conservation in the external shockwave region 2*

$$\frac{dE_2}{dt} = 4\pi p_c R_c^{\,2}\dot{R}_c + 4\pi R_{e'}^{\,2}\left(\dot{R}_{e'} - u_{e1'}\right)\left[\frac{\gamma_g p_g}{\gamma_g - 1} + \frac{1}{2}\rho_{e1'}u_{e1'}^{\,2}\right], \text{ with } \quad E_{e2} = E_{e2t} + E_{e2k} \tag{3.9}$$

Besides the above nine equations, the pressure within the internal shockwave region is assumed to be uniform during this stage and is equal to the pressure of external

shockwave region adjacent to the contact surface as

$$p_i = p_c \tag{3.10}$$

In the present study, the existence of the refracted shockwave inside the external shockwave region (cf. fig. 1c) is not a dominant mechanism in determining the evolution of the vapor plume (due to the weakness of the refracted shockwave compared to the other coexisting shockwaves). An acceptable approximation takes the rate of change of the density, pressure, and velocity within the two regions separated by the refracted shockwave to be equal (the three additional relations are given below for this case). These relations simplify the calculations and also guarantee that the density, pressure, and velocity inside the external shockwave regions are linear functions, which is consistent with the simulations in stage 2 and stage 4, even when the refracted shockwave degenerates into a sound wave.

$$\frac{u_{e1} - u_{e1'}}{R_e - R_{e'}} = \frac{u_{e2'} - \dot{R}_c}{R_{e'} - R_c}; \quad \frac{p_{e1} - p_{e1'}}{R_e - R_{e'}} = \frac{p_{e2'} - p_c}{R_{e'} - R_c}; \quad \frac{\rho_{e1} - \rho_{e1'}}{R_e - R_{e'}} = \frac{\rho_{e2'} - \rho_{e2}}{R_{e'} - R_c} \tag{3.11a,b,c}$$

Stage Four

Stage four starts after the internal shockwave disappears in the vapor plume.

In this last stage of the simulation, the strength of the internal shockwave within the vapor plume is weak and can be neglected. The system is composed of a high temperature uniform vapor plume and an external shockwave region. The propagation speed of the external shockwave gradually diminished and approaches the sound speed in the background gas. Accordingly, the pressure in the external shockwave region (cf. fig. 1d and 5) is close to atmospheric pressure. Pressure, density, and temperature are treated to be uniform inside the vapor plume. The corresponding variables in the external shockwave region (cf. fig. 5) are treated as linear functions

since this region is large compared to the vapor plume in this stage. Again, the velocities in both regions are approximated by linear functions (cf. fig. 5). Conservation laws within the vapor plume and the external shockwave regions are used to construct the necessary relations in this stage.

- *Mass conservation in the vapor plume region*
-

$$M_v = M = \rho_p \frac{4\pi}{3} R_c^{\,3} \tag{4.1}$$

- *Energy conservation in the vapor plume*

$$\frac{dE_v}{dt} = -4\pi R_c^{\,2} \dot{R}_c p_c \,, \text{ with } \; E_v = E_{vt} + E_{vk} \tag{4.2}$$

- *Mass conservation in the external shockwave region*

$$M_e = \frac{4\pi}{3} R_e^{\,3} \rho_g \tag{4.3}$$

- *Momentum conservation in the external shockwave region*

$$\begin{aligned} \frac{dP_e}{dt} &= \pi R_c^{\,2} p_c - \pi R_e^{\,2} p_g + \int_{R_c}^{R_e} p 2\pi r dr \\ &= \pi R_c^{\,2} p_c - \pi R_e^{\,2} p_g + 2\pi \left[\left(\frac{p_{e1} - p_c}{R_e - R_c} \right) \frac{1}{3} \left(R_e^{\,3} - R_c^{\,3} \right) + \left(\frac{R_e p_c - R_c p_{e1}}{R_e - R_c} \right) \frac{1}{2} \left(R_e^{\,2} - R_c^{\,2} \right) \right] \end{aligned} \tag{4.4}$$

- *Energy conservation in the external shockwave region*
-

$$E_e = E_{laser} + \frac{4\pi}{3} \frac{p_g}{\gamma_g - 1} R_e^{\,3} - E_v \,, \text{ with } \; E_e = E_{et} + E_{ek} \tag{4.5}$$

Results and discussion

The simulated and experimental results [11] for the trajectories of the contact surface and the internal and external shockwaves are shown in Figs. 6 and 7. The total laser energy (E) transferred to the vapor plume (vaporized sample) and to the background gas and the mass (M) of the sample that is vaporized are determined by the comparison of the experimental data with the numerical results. The simulated M's are qualitatively consistent with the experimental results from the measurement of crater volumes (which directly relates to the vaporized sample mass) for ablation with two different laser energies, E=10 and 30mJ (cf. fig. 8). The larger deviation between the simulated M and the experimental data for E=10mJ results from the difficulty in determining the contribution of the measured upper volume to the net volume. Part of the upper volume comes from the residue of the deposition of the vaporized mass which should be excluded in the vaporized mass measurement but which is difficult to subtract.

The value of *E* evaluated from these simulations is larger than the value obtained using Sedov's (E_{sedov}) similarity solution:

$$R_{external} = \left(\frac{E_{sedov}}{\rho_{gas}} \right)^{1/5} t^{2/5} \qquad (5.1)$$

E_{sedov} is not equal to the total laser energy transferred to the vapor plume and to the background gas. The density, pressure, temperature, and velocity distributions for a real laser ablation system differ from Sedov's solution. Also, the kinetic and thermal energies in the vapor plume are not included in E_{sedov}. The presence of a vapor plume and a significant interaction between the vapor plume and the background gas are not considered in Sedov's solution. Based on our simulation, when the external shockwave is far from the vapor plume (~50ns after laser pulse), ~80% of the energy of the gas is in the compressed background gas region behind the external shockwave, and ~20% of the absorbed laser energy is in the vapor plume. In addition, rather than

0.4 in the exponent of time in Eq. (5.1), the present analysis shows that the time exponent in Eq. (5.1) should be slightly larger at ~0.42, which shows better agreement with the experimental data (Table 1).

In addition to the external shockwave formed when the vapor plume expands into the background gas, an internal shockwave also is formed in the vapor plume. This shockwave balances the velocity and high backpressure generated by the external shockwave when the vapor plume expands supersonically. This internal shockwave reflects back and forth within the vapor plume until the vapor plume expansion slows down. This effect is manifested in the line emission images [11], where a high emission region of the vapor plume moves back and forth inside the vapor plume. From both the current simulation and the experimental data, only two internal shockwave reflections can be observed. From the simulation, the first time when the internal shockwave strikes the sample is ~10 ns after the end of the laser pulse. The second internal shockwave hits the surface at ~50 ns after laser pulse. These times depend on the background gas and the laser energy.

The Mach number of the reflected shockwave, M_R, is related to the Mach number of the incident shockwave, M_S, according to [12]

$$\frac{M_R}{M_R^2-1}=\frac{M_S}{M_S^2-1}\sqrt{1+\frac{2(\gamma_v-1)}{(\gamma_v+1)^2}(M_s^2-1)\left(\gamma_v+\frac{1}{M_s^2}\right)} \qquad (5.2)$$

where γ_v is the specific heat ratio of the vapor plume, which is $5/3$ in our experiments. The maximum possible value of M_R (with $M_S \to \infty$) is $M_R = 2.236$. This means the strength of the shockwave is reduced significantly after each reflection and may be the reason why there are only two internal shockwave reflections obtained in the present analysis.

Density and pressure vary with position within the vapor plume. These two physical properties at the contact surface are plotted as functions of time after the laser pulse

(cf. Fig. 9 and 10). The temperature and electron number density of the vapor plume are not explicitly modeled in the analysis. They are evaluated from the pressure and density by the following relations

$$T_c = \frac{p_c}{\rho_c (1+\alpha)\Re_p} \qquad (5.3)$$

with

$$\alpha = \frac{n_a + n_e}{n_a}, \quad n_a = \sum_{i=0}^{\infty} n_i \text{, and } \quad n_e = \sum_{i=0}^{\infty} i n_i \qquad (5.4)$$

The electron density can be evaluated from Saha's equation by the assumption of a local thermal equilibrium (LTE),

$$\frac{n_e n_i}{n_i} = \frac{2Q_{i+1}}{Q_i}\left(\frac{2\pi m_e kT}{h^2}\right)^{3/2} e^{-\varepsilon_{i+1}/kT} \qquad (5.5)$$

The simulated values of T_c, ρ_c, and p_c are shown in Fig. 9-12.

The simulated density, pressure, and electron number density of the vapor plume change almost linearly on the log-log plots (cf. figs. 9-12), which is qualitatively consistent with experimental results for silicon [13]. The pressure of the vapor plume decreases to the same magnitude as the background gas for times greater than $1\mu s$ after the laser pulse for both laser energies. From these data, we can assume that the vapor plume reaches a gas dynamic equilibrium with the ambient gas at these times. This conclusion greatly simplifies the analysis of plasma emission from the vapor plume at times greater than $1\mu s$ after the laser pulse since the pressure can be assumed to be the same as the background gas pressure based on the present study [11]; this is especially important for the chemical analysis (e.g. laser induced breakdown spectroscopy, LIBS) which depends on the longtime spectral line emission which is a strong function of the temperature and pressure of the vapor plume. The temperature of the vapor plume does not decrease monotonically as a function of time during the first 100ns. Instead, the deceleration of the rapidly expanding vapor plume

converts kinetic energy to thermal energy of the vapor plume during this time [14]. After this time, most of the kinetic energy has been converted to thermal energy of the vapor plume and the temperature, density, pressure, and electron number density of the vapor plume start to decrease with time accompanied with the expansion of the vapor plume. At $1\mu s$, temperatures predicted in the simulations are about three times greater than the experimental results [11]. This discrepancy could be due to the shockwave jump conditions used in this work which are valid for ideal gases but do not include the ionization energy of the vapor plume. A closed form solution of the jump conditions as a function of the upstream conditions can not be achieved for shockwave propagation in the highly ionized vapor plume [15]. Therefore, an iterative algorithm should be used in the calculation of the jump conditions after the shockwave for a highly ionized vapor plume. Another possible reason for the overestimate of the simulated value of the temperature of the vapor plume is the exclusion of the thermal radiation in the present study [11]. This simplification is valid as long as the thermal radiation is not the dominate source of energy loss from the vapor plume [16]. Besides, there are discontinuities in pressure, density, electron number density, and temperature at ~10ns and at ~100ns after the laser pulse. These times correspond to when the internal shockwave strikes the contact surface and induces a sudden increase in all these physical properties.

Heat losses by conduction or radiation are not considered in the analysis. In the first 1 μ s after the laser pulse, conductive and diffusive heat transfer are not significant compared to the total thermal energy in the vapor plume in the first 1 μ s after laser pulse [13]. For thermal radiation, continuum emission is small compared to the total thermal energy and line emission is not fully developed during the first few 100ns after the laser pulse; the transition probabilities of most lines are small ~ $\leq 10^7 (s^{-1})$.

Thus, radiative heat transfer also can be neglected and the vapor plume can be considered as undergoing an adiabatic expansion ~ 100's ns after the laser pulse. Radiative heat loss primarily influences the expansion and temperature of the vapor plume (which caused the discrepancy between the simulated and experimental temperature at $1\mu s$ as discussed above), but not the propagation of the shockwaves. The external shockwave detaches from the vapor plume before ~100 ns when radiative heat loss from the vapor plume is not important and the temperature of the compressed gas layer is not high enough to produce significant radiative heat loss (compared to the p-v work by the vapor plume on the background gas).

Conclusion

An analysis was made to describe the laser energy coupling to a gas and the amount of vaporized mass in the vapor plume during ablation. Mass, momentum, and energy conservation equations were solved in all regions affected by the laser energy transport. The integrated conservation equations were used and linear variations of the variables were assumed. The present simulation is time efficient and is demonstrated to be a useful, tractable approach to determine the propagation of the internal shockwave, contact surface, and the external shockwave along with the variables in all of the regions. The analysis permits the determinations of the laser energy conversion efficiency and the amount of sample vaporized (both are dominant parameters of the laser ablation process and are difficult to obtain from the previous studies) by comparing the simulated trajectories of the external shockwave and the contact surface with the experimental results. For the present conditions ($\lambda = 1064nm$, spot size $\sim 300\mu m$, pulse length ~ 4ns), the laser energy conversion efficiency for ablation in Ar [3] is 30-40%, and the vaporized mass is $5.5\times10^{-12}kg$ for E=10mJ

and is $1.3\times10^{-11}kg$ for E=30mJ for each laser pulse. These values correspond to the same order as the crater volume measured after each laser ablation for both laser energies [3]. The laser energy conversion efficiency evaluated was greater than that evaluated from Sedov's law. Sedov's law only describes the energy of the external shockwave, which is less than the total energy stored in the vapor plume and shockwave regions.

The density, pressure, temperature, and electron density within the vapor plume were determined as functions of time as along as the laser energy conversion efficiency and the amount of sample mass vaporized are known. The four physical properties show linear decreases with respect to time in log-log plots after the vapor plume detaches from the external shockwave, in qualitative agreement with experiments. The information about the time evolution of the density, pressure, temperature, and electron density within the vapor plume is important for phenomena sensitive to the early expansion of the vapor plume. These include production of soft x-rays from the laser plasma, laser propulsion and laser ultrasonic generation.

Acknowledgment

This work was supported by the U.S. Department of Energy, Office of Basic Energy Sciences, Chemical Sciences Division at the Lawrence Berkeley National Laboratory under contract number DE-AC02-05CH11231. The authors would like to thank Dr. Paul Berdahl for the valuable discussion in preparing the manuscript.

Nomenclature

c_p	Specific heat with constant pressure

c_v	Specific heat with constant volume
E	Total energy in the vapor plume
E_e	Total energy in the external shockwave region
E_{ek}	Kinetic energy in the external shockwave region
E_{et}	Thermal energy in the external shockwave region
E_{e1k}	Kinetic energy in the external shockwave region 1
E_{e1t}	Thermal energy in the external shockwave region 1
E_{e2k}	Kinetic energy in the external shockwave region 2
E_{e2t}	Thermal energy in the external shockwave region 2
E_i	Total energy in the internal shockwave region
E_{ik}	Kinetic energy in the internal shockwave region
E_{it}	Thermal energy in the internal shockwave region
E_p	Total energy in the unshocked vapor plume
E_{pk}	Kinetic energy in the unshocked region
E_{pt}	Thermal energy in the unshocked region
E_v	Total energy in the vapor plume
F_i	$i = 1-5$, defined infinite integral functions
M_e	Compressed air mass in the external shockwave region
M_{e1}	Compressed air mass in the external shockwave region 1
M_{e2}	Compressed air mass in the external shockwave region 2
M_i	Vaporized sample mass in the internal shockwave region
M_p	Vaporized sample mass in the unshocked plume region
n_e	Electron density of the vapor plume at the contact surface
n_i	*i*th order ionized atom density
p_c	Pressure of the vapor plume at the contact surface
P_e	Momentum in the external shockwave region
p_e	Pressure after the external shockwave
P_i	Momentum in the internal shockwave region
p_i	Pressure after the internal shockwave
P_p	Momentum in the unshocked region
Q_i	Partition function at *i*th ionized stage
R	Radius of plume neglecting the ambient gas
R_c	Position of the contact surface
R_e	Position of the external shockwave front
$R_{e'}$	Position of the refracted shockwave in the external shockwave region
R_i	Position of the internal shockwave front
R_o	Initial plume radius (Taken as focal radius in the calculation)
$\dot{R}_c$	Velocity of the contact surface

$\dot{R}_e$	Velocity of the external shockwave front
$\dot{R}_{e'}$	Velocity of the refracted shockwave in the external shockwave region
$\dot{R}_i$	Velocity of the internal shockwave front
T_c	Temperature of the vapor plume at the contact surface
T_g	Temperature of the background air
u_e	Velocity after the external shockwave
u_i	Velocity after the internal shockwave
u_o	Initial plume expansion speed after the laser supplies energy
$V_e(r)$	Velocity in the external shockwave region
ε_i	Ionization potential of *i*th ionized stage of the vapor
γ_g	Specific heat ratio of the background air
γ_p	Specific heat ratio of the plume
ρ_c	Density of the vapor plume at the contact surface
ρ_e	Density after the external shockwave
ρ_g	Background air density
$\xi = r/R$	Dimensionless Lagrange position in the vapor plume
$\Re_p$	Gas constant of vapor plume
$\Re_g$	Gas constant of background gas

Appendix

Stage one:

$$M_p = \int_0^{R_i} \rho_p 4\pi r^2 dr = 4\pi\rho_o \Psi(t)^{-3/2} R^3 F_1\left[\frac{R_i}{R}\right] \tag{A.1}$$

$$M_i = \frac{4\pi}{3}\left(R_c^{\,3} - R_i^{\,3}\right)\frac{\gamma_p + 1}{\gamma_p - 1}\rho_{R_i} = \frac{4\pi}{3}\left(R_c^{\,3} - R_i^{\,3}\right)\frac{\gamma_p + 1}{\gamma_p - 1}\rho_o\left[1 - \left(\frac{R_i}{R}\right)^2\right]^{3/2}\Psi(t)^{-3/2} \tag{A.2}$$

$$P_e = \int_{R_c}^{R_e} \rho V \pi r^2 dr = \pi\rho_e\left\{\left(\frac{u_e - \dot{R}_c}{R_e - R_c}\right)\frac{1}{4}\left(R_e^{\,4} - R_c^{\,4}\right) + \left(\frac{R_e\dot{R}_c - R_c u_e}{R_e - R_c}\right)\frac{1}{3}\left(R_e^{\,3} - R_c^{\,3}\right)\right\} \tag{A.3}$$

$$E_{pt} = \int_0^{R_i} \frac{1}{\gamma_p - 1} p_p 4\pi r^2 dr = \frac{1}{\gamma_p - 1} 4\pi\rho_o \Re_p T_o \Psi(t)^{-5/2} R^3 F_3\left[\frac{R_i}{R}\right] \tag{A.4}$$

$$E_{pk} = \int_0^{R_i} \rho_p \frac{V_p^{\,2}}{2} 4\pi r^2 dr = 2\rho_o \Psi(t)^{-3/2} R_o^{\,2} \Phi(t)^2 \pi R^3 F_2\left[\frac{R_i}{R}\right] \tag{A.5}$$

$$E_{it} = \int_{R_i}^{R_c} \frac{p_c}{\gamma_p - 1} 4\pi r^2 dr = \frac{p_c}{\gamma_p - 1}\frac{4\pi}{3}\left(R_c^{\,3} - R_i^{\,3}\right) \tag{A.6}$$

$$E_{ik} = \int_{R_i}^{R_c} \rho_i \frac{V_i^2}{2} 4\pi r^2 dr = 2\pi\left[\frac{1}{3}\left(\frac{R_c u_i - R_i\dot{R}_c}{R_c - R_i}\right)^2\left(R_c^{\,3} - R_i^{\,3}\right) + \frac{1}{2}\frac{R_c u_i - R_i\dot{R}_c}{R_c - R_i}\frac{\dot{R}_c - u_i}{R_c - R_i}\left(R_c^{\,4} - R_i^{\,4}\right) + \frac{1}{5}\left(\frac{\dot{R}_c - u_i}{R_c - R_i}\right)^2\left(R_c^{\,5} - R_i^{\,5}\right)\right] \cdot$$
$$\frac{\gamma_p + 1}{\gamma_p - 1}\rho_o\left[1 - \left(\frac{R_i}{R}\right)^2\right]^{3/2}\Psi(t)^{-3/2} \tag{A.7}$$

$$E_{et} = \int_{R_c}^{R_e} \frac{1}{\gamma_p - 1} p 4\pi r^2 dr = \frac{4\pi}{\gamma_p - 1}\left[\frac{p_{e1} - p_c}{R_e - R_c}\frac{1}{4}\left(R_e^{\,4} - R_c^{\,4}\right) + \frac{R_e p_c - R_c p_{e1}}{R_e - R_c}\frac{1}{3}\left(R_e^{\,3} - R_c^{\,3}\right)\right] \tag{A.8}$$

$$E_{ek} = \int_{R_c}^{R_e} \rho\frac{V^2}{2} 4\pi r^2 dr$$
$$= 2\pi\rho_e\left\{\left(\frac{u_e - \dot{R}_c}{R_e - R_c}\right)^2\frac{1}{5}\left(R_e^{\,5} - R_c^{\,5}\right) + 2\left(\frac{u_e - \dot{R}_c}{R_e - R_c}\right)\left(\frac{R_e\dot{R}_c - R_c u_e}{R_e - R_c}\right)\frac{1}{4}\left(R_e^{\,4} - R_c^{\,4}\right) + \left(\frac{R_e\dot{R}_c - R_c u_e}{R_e - R_c}\right)^2\frac{1}{3}\left(R_e^{\,3} - R_c^{\,3}\right)\right\} \tag{A.9}$$

- *Jump conditions across the internal shockwave* [7]

$$\rho_i = \frac{\gamma_p + 1}{\gamma_p - 1}\left(1 + \frac{2}{\gamma_p - 1}\frac{\gamma_p \Re_p T_{R_i}}{\left(\dot{R}_i - V_{R_i}\right)^2}\right)^{-1} \rho_{R_i} \tag{A.10}$$

$$p_i = \frac{2}{\gamma_p + 1}\rho_{R_i}\left(\dot{R}_i - V_{R_i}\right)^2\left(1 - \frac{\gamma_p - 1}{2\gamma_p}\frac{\gamma_p \Re_p T_{R_i}}{\left(\dot{R}_i - V_{R_i}\right)^2}\right) \tag{A.11}$$

$$u_i = \frac{2}{\gamma_p + 1}\left(\dot{R}_i - V_{R_i}\right)\left(1 - \frac{\gamma_p \Re_p T_{R_i}}{\left(\dot{R}_i - V_{R_i}\right)^2}\right) + V_{R_i} \tag{A.12}$$

with the subscript R_i indicating the position just before the internal shockwave where

$$T_{R_i}(t) = T_o\left[1 - \left(\frac{R_i}{R}\right)^2\right]\Psi(t)^{-1};\ \rho_{R_i}(t) = \rho_o\left[1 - \left(\frac{R_i}{R}\right)^2\right]^{3/2}\Psi(t)^{-3/2};\ V_{R_i}(t) = \frac{R_i}{R}R_o\Phi(t)$$

- *Jump conditions across the external shockwave*

$$\rho_e = \frac{\gamma_g + 1}{\gamma_g - 1}\rho_g\left[1 + \frac{2}{\gamma_g - 1}\frac{\gamma_g \Re_g T_g}{\dot{R}_e^{\,2}}\right]^{-1} \tag{A.13}$$

$$p_e = \frac{2}{\gamma_g + 1}\rho_g \dot{R}_e^{\,2}\left[1 - \frac{\gamma_g - 1}{2\gamma_g}\frac{\gamma_g \Re_g T_g}{\dot{R}_e^{\,2}}\right] \tag{A.14}$$

$$u_e = \frac{2}{\gamma_g + 1}\dot{R}_e\left(1 - \frac{\gamma_g \Re_g T_g}{\dot{R}_e^{\,2}}\right) \tag{A.15}$$

Stage two:

$$P_p = \int_{R_c}^{R_e} \rho_p V \pi r^2 dr = \rho_p \pi\left[\left(\frac{u_p - \dot{R}_c}{R_e - R_c}\right)\frac{1}{4}\left(R_e^{\,4} - R_c^{\,4}\right) + \left(\frac{R_e\dot{R}_c - R_c u_p}{R_e - R_c}\right)\frac{1}{3}\left(R_e^{\,3} - R_c^{\,3}\right)\right] \tag{A.16}$$

$$E_{pt} = \int_{R_i}^{R_c} \rho_p c_v T_p 4\pi r^2 dr = \frac{p_c}{\gamma_p - 1}\frac{4\pi}{3}\left(R_c^{\,3} - R_i^{\,3}\right) \tag{A.17}$$

$$E_{pk}=\int_{R_i}^{R_c}\rho_p\frac{V^2}{2}4\pi r^2dr=2\rho_p\pi\left[\left(\frac{R_cu_p-R_i\dot{R}_c}{R_c-R_i}\right)^2\frac{\left(R_c{}^3-R_i{}^3\right)}{3}+\left(\frac{R_cu_p-R_i\dot{R}_c}{R_c-R_i}\right)\left(\frac{\dot{R}_c-u_p}{R_c-R_i}\right)\frac{\left(R_c{}^4-R_i{}^4\right)}{2}+\left(\frac{\dot{R}_c-u_p}{R_c-R_i}\right)^2\frac{\left(R_c{}^5-R_i{}^5\right)}{5}\right]$$

(A.18)

$$M_i=\frac{4\pi}{3}\rho_iR_i{}^3 \tag{A.19}$$

$$E_{it}=\int_0^{R_i}\frac{1}{\gamma_p-1}p_i4\pi r^2dr=\frac{4\pi}{3}\frac{1}{\gamma_p-1}R_i{}^3\frac{2}{\gamma_p+1}\rho_p\left(\dot{R}_i-u_p\right)^2\left(1-\frac{\gamma_p-1}{2\gamma_p}\frac{\gamma_p\Re_pT_p}{\left(\dot{R}_i-u_p\right)^2}\right)$$

(A.20)

$$E_{ik}=\int_0^{R_i}\rho_i\frac{V^2}{2}4\pi r^2dr=\frac{2\pi R_i{}^3}{5}\frac{M_i}{\frac{4\pi}{3}R_i{}^3}\left[\frac{2}{\gamma_p+1}\left(\dot{R}_i-u_p\right)\left(1-\frac{\gamma_p\Re_pT_p}{\left(\dot{R}_i-u_p\right)^2}\right)+u_p\right]^2 \tag{A.21}$$

$$P_e=\int_{R_c}^{R_e}\rho V\pi r^2dr=\pi\rho_e\left\{\left(\frac{u_e-\dot{R}_c}{R_e-R_c}\right)\frac{1}{4}\left(R_e{}^4-R_c{}^4\right)+\left(\frac{R_e\dot{R}_c-R_cu_e}{R_e-R_c}\right)\frac{1}{3}\left(R_e{}^3-R_c{}^3\right)\right\} \tag{A.22}$$

$$E_{et}=\int_{R_c}^{R_e}\frac{1}{\gamma_p-1}p4\pi r^2dr=\frac{4\pi}{\gamma_p-1}\left[\frac{p_e-p_c}{R_e-R_c}\frac{1}{4}\left(R_e{}^4-R_i{}^4\right)+\frac{R_ep_c-R_cp_e}{R_e-R_c}\frac{1}{3}\left(R_e{}^3-R_i{}^3\right)\right]$$

(A.23)

$$E_{ek}=\int_{R_c}^{R_e}\rho\frac{V^2}{2}4\pi r^2dr$$

$$=2\pi\rho_e\left\{\left(\frac{u_e-\dot{R}_c}{R_e-R_c}\right)^2\frac{1}{5}\left(R_e{}^5-R_c{}^5\right)+\left(\frac{u_e-\dot{R}_c}{R_e-R_c}\right)\left(\frac{R_e\dot{R}_c-R_cu_e}{R_e-R_c}\right)\frac{1}{2}\left(R_e{}^4-R_c{}^4\right)+\left(\frac{R_e\dot{R}_c-R_cu_e}{R_e-R_c}\right)^2\frac{1}{3}\left(R_e{}^3-R_c{}^3\right)\right\}$$

(A.24)

- *Jump conditions across the internal shockwave*

$$p_i=\frac{2}{\gamma_p+1}\rho_p\left(\dot{R}_i-u_p\right)^2\left(1-\frac{\gamma_p-1}{2\gamma_p}\frac{\gamma_p\Re_pT_p}{\left(\dot{R}_i-u_p\right)^2}\right) \tag{A.25}$$

$$u_i=\frac{2}{\gamma_p+1}\left(\dot{R}_i-u_p\right)\left(1-\frac{\gamma_p\Re_pT_p}{\left(\dot{R}_i-u_p\right)^2}\right)+u_p \tag{A.26}$$

- *Jump conditions across the external shockwave*

$$\rho_e = \frac{\gamma_g + 1}{\gamma_g - 1}\rho_g \left[1 + \frac{2}{\gamma_g - 1}\frac{\gamma_g R_g T_g}{\dot{R}_e^{\,2}} \right]^{-1} \tag{A.27}$$

$$p_e = \frac{2}{\gamma_g + 1}\rho_g \dot{R}_e^{\,2} \left[1 - \frac{\gamma_g - 1}{2\gamma_g}\frac{\gamma_g R_g T_g}{\dot{R}_e^{\,2}} \right] \tag{A.28}$$

$$u_e = \frac{2}{\gamma_g + 1}\dot{R}_e \left(1 - \frac{\gamma_g R_g T_g}{\dot{R}_e^{\,2}} \right) \tag{A.29}$$

Stage three:

$$E_{pk} = \int_0^{R_i} \rho_p \frac{V^2}{2} 4\pi r^2 dr = \frac{2\pi}{5}\rho_p u_p^{\,2} R_i^{\,3} \tag{A.30}$$

$$E_{pt} = \int_0^{R_i} \frac{1}{\gamma_p - 1} p_p 4\pi r^2 dr = \frac{p_p}{\gamma_p - 1}\frac{4\pi}{3} R_i^{\,3} \tag{A.31}$$

$$E_{ik} = \int_{R_i}^{R_c} \rho_i \frac{V_i^2}{2} 4\pi r^2 dr = 2\pi \left[\frac{1}{3}\left(\frac{R_c u_i - R_i \dot{R}_c}{R_c - R_i} \right)^2 \left(R_c^{\,3} - R_i^{\,3} \right) + \frac{1}{2}\frac{R_c u_i - R_i \dot{R}_c}{R_c - R_i}\frac{\dot{R}_c - u_i}{R_c - R_i}\left(R_c^{\,4} - R_i^{\,4} \right) + \frac{1}{5}\left(\frac{\dot{R}_c - u_i}{R_c - R_i} \right)^2 \left(R_c^{\,5} - R_i^{\,5} \right) \right] \cdot$$
$$\frac{\gamma_p + 1}{\gamma_p - 1}\rho_o \left[1 - \left(\frac{R_i}{R} \right)^2 \right]^{3/2} \Psi(t)^{-3/2} \tag{A.32}$$

$$E_{it} = \int_{R_i}^{R_c} \frac{p_c}{\gamma_p - 1} 4\pi r^2 dr = \frac{p_c}{\gamma_p - 1}\frac{4\pi}{3}\left(R_c^{\,3} - R_i^{\,3} \right) \tag{A.33}$$

$$M_{e1} = \int_{R_{e'}}^{R_e} \rho_e 4\pi r^2 dr = \rho_{e1}\frac{4\pi}{3}\left(R_e^{\,3} - R_{e'}^{\,3} \right) \tag{A.34}$$

$$M_{e2} = \int_{R_c}^{R_{e'}} \rho 4\pi r^2 dr = \rho_{e2}\frac{4\pi}{3}\left(R_{e'}^{\,3} - R_c^{\,3} \right) \tag{A.35}$$

$$P_e = \int_{R_c}^{R_{e'}} \rho V \pi r^2 dr + \int_{R_{e'}}^{R_e} \rho V \pi r^2 dr$$
$$= \pi\rho_{e2}\left\{ \left(\frac{u_{e2'} - \dot{R}_c}{R_{e'} - R_c} \right)\frac{1}{4}\left(R_{e'}^{\,4} - R_c^{\,4} \right) + \left(\frac{R_{e'}\dot{R}_c - R_c u_{e2'}}{R_{e'} - R_c} \right)\frac{1}{3}\left(R_{e'}^{\,3} - R_c^{\,3} \right) \right\} + \tag{A.36}$$
$$\pi\rho_{e1}\left\{ \left(\frac{u_{e1} - u_{e1'}}{R_e - R_{e'}} \right)\frac{1}{4}\left(R_e^{\,4} - R_{e'}^{\,4} \right) + \left(\frac{R_e u_{e1'} - R_{e'} u_{e1}}{R_e - R_{e'}} \right)\frac{1}{3}\left(R_e^{\,3} - R_{e'}^{\,3} \right) \right\}$$

$$E_{e1t} = \int_{R_{e'}}^{R_e} \frac{1}{\gamma_p - 1} p 4\pi r^2 dr = \frac{4\pi}{\gamma_p - 1}\left[\frac{p_{e1} - p_{e1'}}{R_e - R_{e'}} \frac{1}{4}\left(R_e^{\,4} - R_{e'}^{\,4} \right) + \frac{R_e p_{e1'} - R_{e'} p_{e1}}{R_e - R_{e'}} \frac{1}{3}\left(R_e^{\,3} - R_{e'}^{\,3} \right) \right]$$

(A.37)

$$E_{e1k} = \int_{R_{e'}}^{R_e} \rho \frac{V^2}{2} 4\pi r^2 dr$$

$$= 2\pi\rho_{e1}\left\{ \left(\frac{u_{e1} - u_{e1'}}{R_e - R_{e'}} \right)^2 \frac{1}{5}\left(R_e^{\,5} - R_{e'}^{\,5} \right) + \left(\frac{u_{e1} - u_{e1'}}{R_e - R_{e'}} \right)\left(\frac{R_e u_{e1'} - R_{e'} u_{e1}}{R_e - R_{e'}} \right) \frac{1}{2}\left(R_e^{\,4} - R_{e'}^{\,4} \right) + \left(\frac{R_e u_{e1'} - R_{e'} u_{e1}}{R_e - R_{e'}} \right)^2 \frac{1}{3}\left(R_e^{\,3} - R_{e'}^{\,3} \right) \right\}$$

(A.38)

$$E_{e2t} = \int_{R_c}^{R_{e'}} \frac{1}{\gamma_p - 1} p 4\pi r^2 dr = \frac{4\pi}{\gamma_p - 1}\left[\frac{p_{e2'} - p_c}{R_{e'} - R_c} \frac{1}{4}\left(R_{e'}^{\,4} - R_c^{\,4} \right) + \frac{R_{e'} p_c - R_c p_{e2'}}{R_{e'} - R_c} \frac{1}{3}\left(R_{e'}^{\,3} - R_c^{\,3} \right) \right]$$

(A.39)

$$E_{e2k} = \int_{R_c}^{R_{e'}} \rho \frac{V^2}{2} 4\pi r^2 dr$$

$$= 2\pi\rho_{e2}\left\{ \left(\frac{u_{e2'} - \dot{R}_c}{R_{e'} - R_c} \right)^2 \frac{1}{5}\left(R_e^{\,5} - R_{e'}^{\,5} \right) + \left(\frac{u_{e2'} - \dot{R}_c}{R_{e'} - R_c} \right)\left(\frac{R_{e'} \dot{R}_c - R_c u_{e2'}}{R_{e'} - R_c} \right) \frac{1}{2}\left(R_e^{\,4} - R_{e'}^{\,4} \right) + \left(\frac{R_{e'} \dot{R}_c - R_c u_{e2'}}{R_{e'} - R_c} \right)^2 \frac{1}{3}\left(R_e^{\,3} - R_{e'}^{\,3} \right) \right\}$$

(A.40)

- Jump condition across the internal shockwave

$$u_i = \frac{2}{\gamma_p + 1}\left(dR_i - u_p \right)\left[1 - \frac{\gamma_p R_p T_p}{\left(dR_i - u_p \right)^2} \right] + u_p \tag{A.41}$$

$$p_i = \frac{2}{\gamma_p + 1}\rho_p \left(dR_i - u_p \right)^2 \left[1 - \frac{\gamma_p - 1}{2\gamma_p} \frac{\gamma_p R_p T_p}{\left(dR_i - u_p \right)^2} \right] \tag{A.42}$$

- *Jump condition across the external shockwave front 1*

$$\rho_{e1} = \frac{\gamma_g + 1}{\gamma_g - 1}\rho_g \left[1 + \frac{2}{\gamma_g - 1} \frac{\gamma_g R_g T_g}{\dot{R}_e^{\,2}} \right]^{-1} \tag{A.43}$$

$$p_{e1} = \frac{2}{\gamma_g + 1}\rho_g \dot{R}_e^{\,2} \left[1 - \frac{\gamma_g - 1}{2\gamma_g} \frac{\gamma_g R_g T_g}{\dot{R}_e^{\,2}} \right] \tag{A.44}$$

$$u_{e1} = \frac{2}{\gamma_g + 1}\dot{R}_e\left(1 - \frac{\gamma_g R_g T_g}{\dot{R}_e^{\,2}}\right) \tag{A.45}$$

- *Jump condition across the external shockwave from 2*

$$\rho_{e2'} = \frac{\gamma_g + 1}{\gamma_g - 1}\rho_{e1'}\left[1 + \frac{2}{\gamma_g - 1}\frac{\gamma_g R_g T_{e1'}}{\left(\dot{R}_{e'} - u_{e1'}\right)^2}\right]^{-1} \tag{A.46}$$

$$p_{e2'} = \frac{2}{\gamma_g + 1}\rho_{e1'}\left(\dot{R}_{e'} - u_{e1'}\right)^2\left[1 - \frac{\gamma_g - 1}{2\gamma_g}\frac{\gamma_g R_g T_{e1'}}{\left(\dot{R}_{e'} - u_{e1'}\right)^2}\right] \tag{A.47}$$

$$u_{e2'} = \frac{2}{\gamma_g + 1}\left(\dot{R}_{e'} - u_{e1'}\right)\left(1 - \frac{\gamma_g R_g T_{e1'}}{\left(\dot{R}_{e'} - u_{e1'}\right)^2}\right) + u_{e1'} \tag{A.48}$$

Stage four:

$$E_{vt} = \int_0^{R_c}\frac{1}{\gamma_p - 1}p_p 4\pi r^2 dr = \frac{4\pi}{3}\frac{p_c}{\gamma_p - 1}R_c^{\,3} \tag{A.49}$$

$$E_{vk} = \int_0^{R_c}\rho_p\frac{V^2}{2}4\pi r^2 dr = \frac{2\pi}{5}\rho_p R_c^{\,3}\dot{R}_c^{\,2} \tag{A.50}$$

$$M_e = \int_{R_c}^{R_e}\rho_e 4\pi r^2 dr = \frac{\rho_{e1} - \rho_{e2}}{R_e - R_c}\pi\left(R_e^{\,4} - R_c^{\,4}\right) + \frac{R_e\rho_{e2} - R_c\rho_{e1}}{R_e - R_c}\frac{4\pi}{3}\left(R_e^{\,3} - R_c^{\,3}\right) \tag{A.51}$$

$$P_e = \int_{R_c}^{R_e}\rho V\pi r^2 dr = \pi\left\{\left(\frac{\rho_{e1} - \rho_{e2}}{R_c - R_i}\right)\left(\frac{u_{e1} - \dot{R}_c}{R_e - R_c}\right)\frac{1}{5}\left(R_e^{\,5} - R_c^{\,5}\right) + \left(\frac{R_e\rho_{e2} - R_c\rho_{e1}}{R_c - R_i}\right)\left(\frac{R_e\dot{R}_c - R_c u_{e1}}{R_e - R_c}\right)\frac{1}{3}\left(R_e^{\,3} - R_c^{\,3}\right) + \left[\left(\frac{\rho_{e1} - \rho_{e2}}{R_c - R_i}\right)\left(\frac{R_e\dot{R}_c - R_c u_{e1}}{R_e - R_c}\right) + \left(\frac{R_e\rho_{e2} - R_c\rho_{e1}}{R_c - R_i}\right)\left(\frac{u_{e1} - \dot{R}_c}{R_e - R_c}\right)\right]\frac{1}{4}\left(R_e^{\,4} - R_c^{\,4}\right)\right\} \tag{A.52}$$

$$E_{et} = \int_{R_c}^{R_e}\frac{1}{\gamma_p - 1}p 4\pi r^2 dr = \frac{4\pi}{\gamma_p - 1}\left[\frac{p_{e1} - p_c}{R_e - R_c}\frac{1}{4}\left(R_e^{\,4} - R_c^{\,4}\right) + \frac{R_e p_c - R_c p_{e1}}{R_e - R_c}\frac{1}{3}\left(R_e^{\,3} - R_c^{\,3}\right)\right] \tag{A.53}$$

$$E_{ek} = \int_{R_c}^{R_e} \rho \frac{V^2}{2} 4\pi r^2 dr = 2\pi \left\{ \left(\frac{u_{e1} - \dot{R}_c}{R_e - R_c} \right)^2 \left(\frac{\rho_{e1} - \rho_{e2}}{R_c - R_i} \right) \frac{1}{6} \left(R_e^{\,6} - R_c^{\,6} \right) + \right.$$
$$\left[\left(\frac{u_{e1} - \dot{R}_c}{R_e - R_c} \right)^2 \left(\frac{R_e \rho_{e2} - R_c \rho_{e1}}{R_c - R_i} \right) + 2 \left(\frac{u_{e1} - \dot{R}_c}{R_e - R_c} \right) \left(\frac{R_e \dot{R}_c - R_c u_{e1}}{R_e - R_c} \right) \left(\frac{\rho_{e1} - \rho_{e2}}{R_c - R_i} \right) \right] \frac{1}{5} \left(R_e^{\,5} - R_c^{\,5} \right) +$$
$$\left[2 \left(\frac{u_{e1} - \dot{R}_c}{R_e - R_c} \right) \left(\frac{R_e \dot{R}_c - R_c u_{e1}}{R_e - R_c} \right) \left(\frac{R_e \rho_{e2} - R_c \rho_{e1}}{R_c - R_i} \right) + \left(\frac{\rho_{e1} - \rho_{e2}}{R_c - R_i} \right) \left(\frac{R_e \dot{R}_c - R_c u_{e1}}{R_e - R_c} \right)^2 \right] \frac{1}{4} \left(R_e^{\,4} - R_c^{\,4} \right) +$$
$$\left. \left(\frac{R_e \rho_{e2} - R_c \rho_{e1}}{R_c - R_i} \right) \left(\frac{R_e \dot{R}_c - R_c u_{e1}}{R_e - R_c} \right)^2 \frac{1}{3} \left(R_e^{\,3} - R_c^{\,3} \right) \right\} \tag{A.54}$$

- *Jump conditions after the external shockwave*

$$\rho_{e1} = \frac{\gamma_g + 1}{\gamma_g - 1} \rho_g \left[1 + \frac{2}{\gamma_g - 1} \frac{\gamma_g R_g T_g}{\dot{R}_e^{\,2}} \right]^{-1} \tag{A.55}$$

$$p_{e1} = \frac{2}{\gamma_g + 1} \rho_g \dot{R}_e^{\,2} \left[1 - \frac{\gamma_g - 1}{2\gamma_g} \frac{\gamma_g R_g T_g}{\dot{R}_e^{\,2}} \right] \tag{A.56}$$

$$u_{e1} = \frac{2}{\gamma_g + 1} \dot{R}_e \left(1 - \frac{\gamma_g R_g T_g}{\dot{R}_e^{\,2}} \right) \tag{A.57}$$

Reference

[1] M. R. Predtechensky and A. P. Mayorov, Applied Superconductivity **1**(10-12), 2011 (1993).

[2] N. Arnold, J. Gruber, and J. Heitz, Applied Physics A-Materials Science & Processing **69**, S87-S93 (1999).

[3] S. I. Anisimov, B. S. Lukyanchuk, and A. Luches, Applied Surface Science **96-8**, 24 (1996).

[4] L. I. Sedov, Similarity and Dimensional Methods in Mechanics, 10th edition (CRC press, Ann Arbor, 1993)

[5] S. B. Wen, X. Mao, R. Greif, and R. E. Russo, Study of the expansion of the vapor plume generated by laser ablation with a background gas – Part B. Experimental Analysis (submitted).

[6] R. Kelly and A. Miotello, Nuclear Instruments & Methods in Physics Research Section B-Beam Interactions with Materials and Atoms **122**(3), 374 (1997).

[7] B. Xu and Y. C. Shin, Journal of Applied Physics **99**(8), 084310 (2006).

[8] S. I. Anisimov, V. V. Zhakhovski, N. A. Inogamov, K. Nishihara, Y. V. Petrov, and V. A. Khokhlov, Journal of Experimental and Theoretical Physics **103**(2), 183 (2006).

[9] Y. B. Zel'dovich and Yu. P. Raizer, in *Physics of Shock Waves and High-Temperature Hydrodynamic Phenomena*, edited by W. D. Hayes and R. F.

Probstein (Academic, London, 1966).

[10] H. Polachek and R. J. Seeger, Physical Review **84**(5), 922 (1951).

[11] S. B. Wen, X. L. Mao, R. Greif, and R. F. Russo, Journal of Applied Physics **100**(5), 053104 (2006).

[12] John D. Anderson, Modern Compressible flow with historical perspective, 3rd edition (Mc Graw Hill, New York, 2002)

[13] X. Zeng, X. L. Mao, R. Greif, and R. E. Russo, Applied Physics A-Materials Science & Processing **80**(2), 237 (2005).

[14] E. M. Lifshitz and L. D. Landau, Fluid Mechanics, 2nd edition (Butterworh-Heinemann, 1987)

[15] C. Michaut, C. Stehle, S. Leygnac, T. Lanz, and L. Boireau, European Physical Journal D **28**(3), 381 (2004).

[16] T. E. Itina, J. Hermann, P. Delaporte, and M. Sentis, Physical Review e **66**(6), 066406 (2002).

Table I. The exponent b of $R_e \propto t^b$ measured from experiment and predicted by Sedov's law and the present analysis

E=10mJ	Experiment	Sedov's law	Present analysis
Exponent b for $R_e \propto t^b$ (t>100ns)	0.427 (±0.001)	0.4	0.423
Error	—	0.027 (6.32%)	0.004 (0.94%)

E=30mJ	Experiment	Sedov's law	Present analysis
Exponent b for $R_e \propto t^b$ (t>100ns)	0.419 (±0.001)	0.4	0.421
Error	—	0.019 (4.75%)	-0.002 (-0.48%)

.

List of Figures

Figure 1. The structure of the simulated model (a) in stage one, (b) in stage two, (c) in stage three, and (d) in stage four

Figure 2. Schematic density, pressure, and velocity distributions

within each region in stage one

Figure 3. Schematic density, pressure, and velocity distributions

within each region in stage two

Figure 4. Schematic density, pressure, and velocity distributions

within each region in stage three

Figure 5. Schematic density, pressure, and velocity distributions

within each region in stage four

Figure 6. Trajectories in Ar for E=10mJ. $E / E_{laser} = 35\%$; $M = 5.5 \times 10^{-12} kg$

(fluence $\approx 14 J / cm^2$)

Figure 7. Trajectories in Ar for E=30mJ. $E / E_{laser} = 31\%$; $M = 1.3 \times 10^{-11} kg$

(fluence $\approx 42 J / cm^2$)

Figure 8. (a) Crater volumes of laser ablations after 200 pulses in different

background gas and laser energy. (b) Sketch of the determination of crater volume

(typical crater profile of the 200 times ablation at same spot in helium for E=30mJ).

Figure 9. Density of the vapor plume at the contact surface for E=10 and 30mJ

(fluence ≈ 14 and $42 J / cm^2$).

Figure 10. Pressure of the vapor plume at the contact surface for E=10 and 30mJ (fluence ≈ 14 and $42 J / cm^2$).

Figure 11. Electron number density of the vapor plume at the contact surface for E=10 and 30mJ (fluence ≈ 14 and $42 J / cm^2$).

Figure 12. Temperature of the vapor plume at the contact surface for E=10 and 30mJ (fluence ≈ 14 and $42 J / cm^2$).

List of Table

Table I. The exponent b of $R_e \propto t^b$ measured from experiment and predicted by Sedov's law and the present analysis

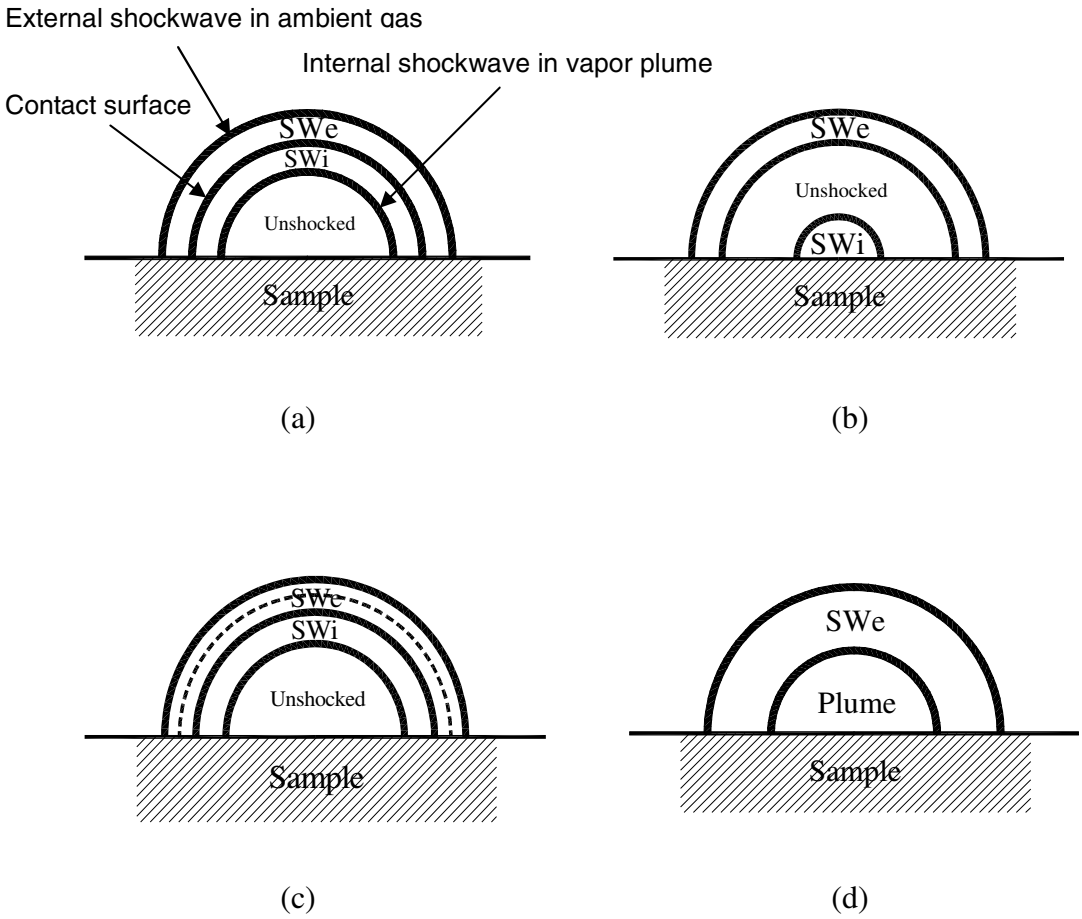
External shockwave in ambient gas
Internal shockwave in vapor plume
Contact surface
SWe
SWi
Unshocked
Sample
(a)
SWe
Unshocked
SWi
Sample
(b)
SWe
SWi
Unshocked
Sample
(c)
SWe
Plume
Sample
(d)

Figure 1

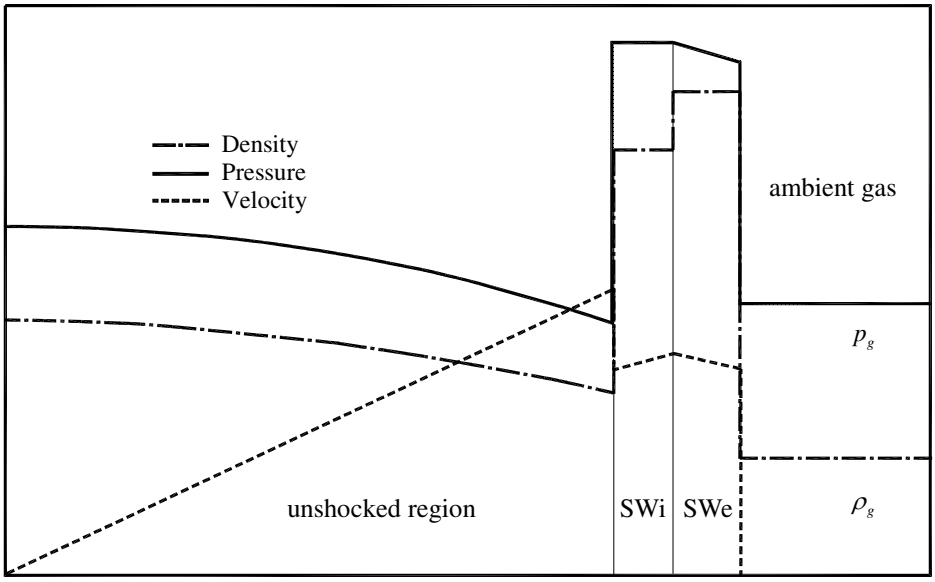

Figure 2

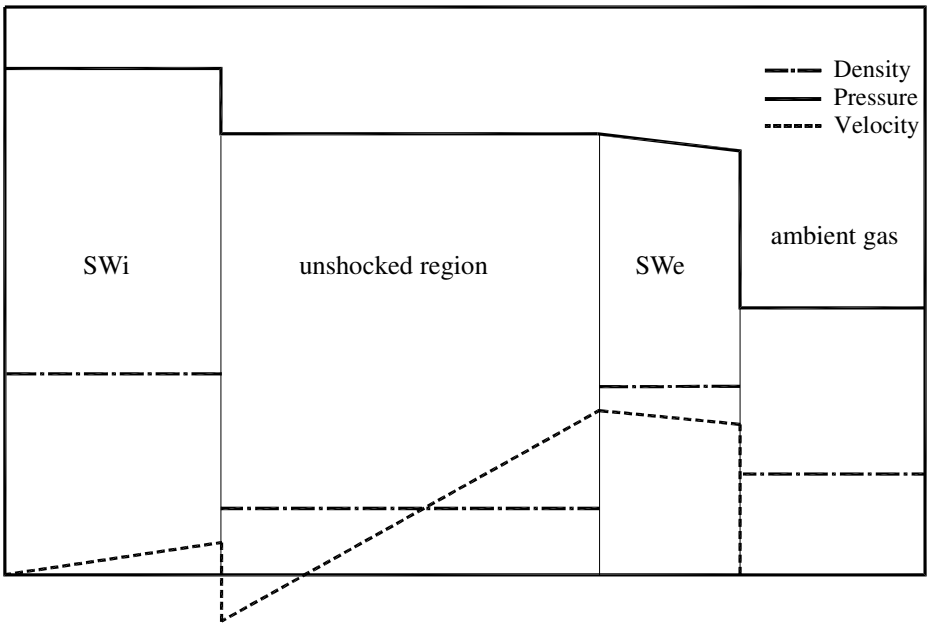

Figure 3

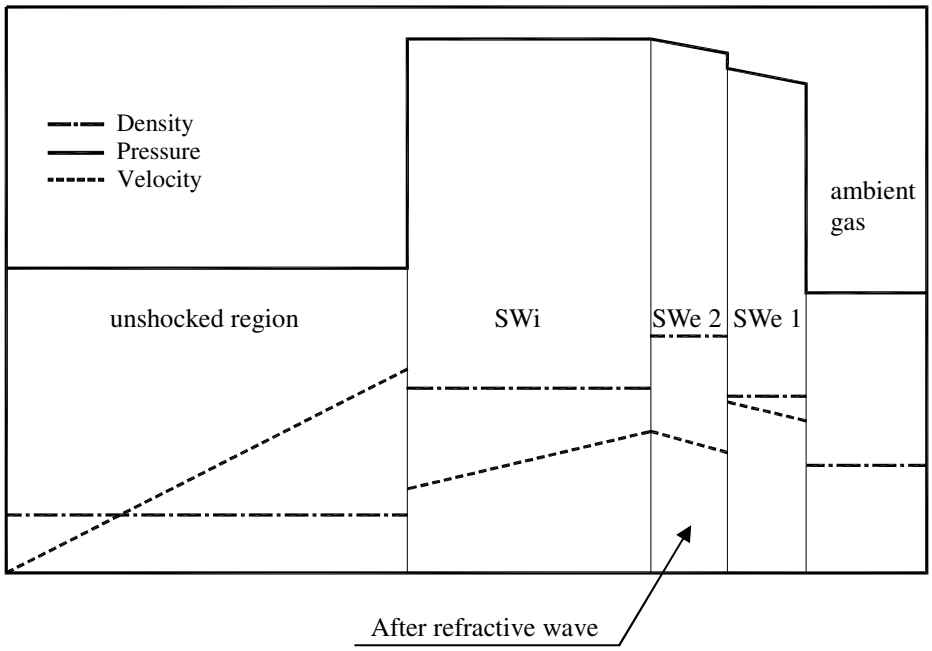

Figure 4

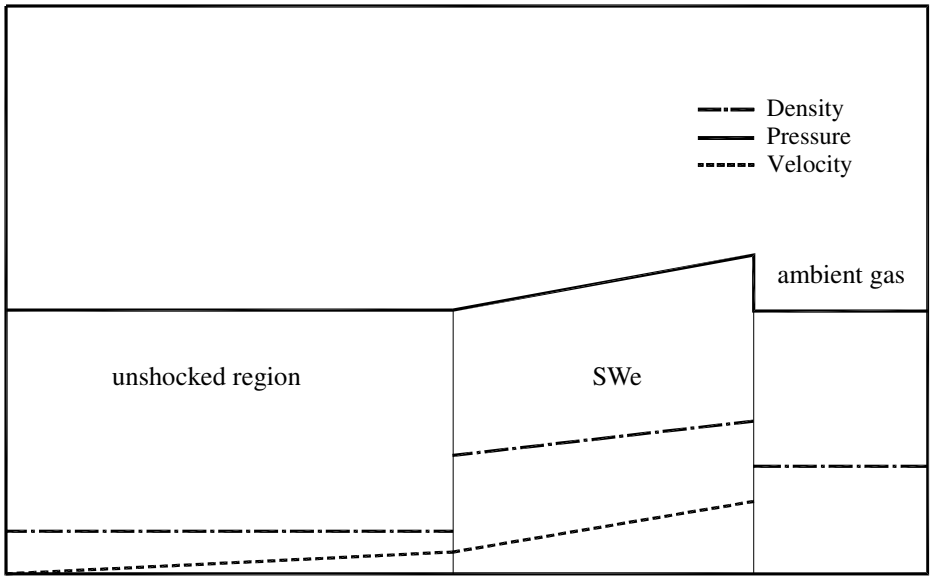

Figure 5

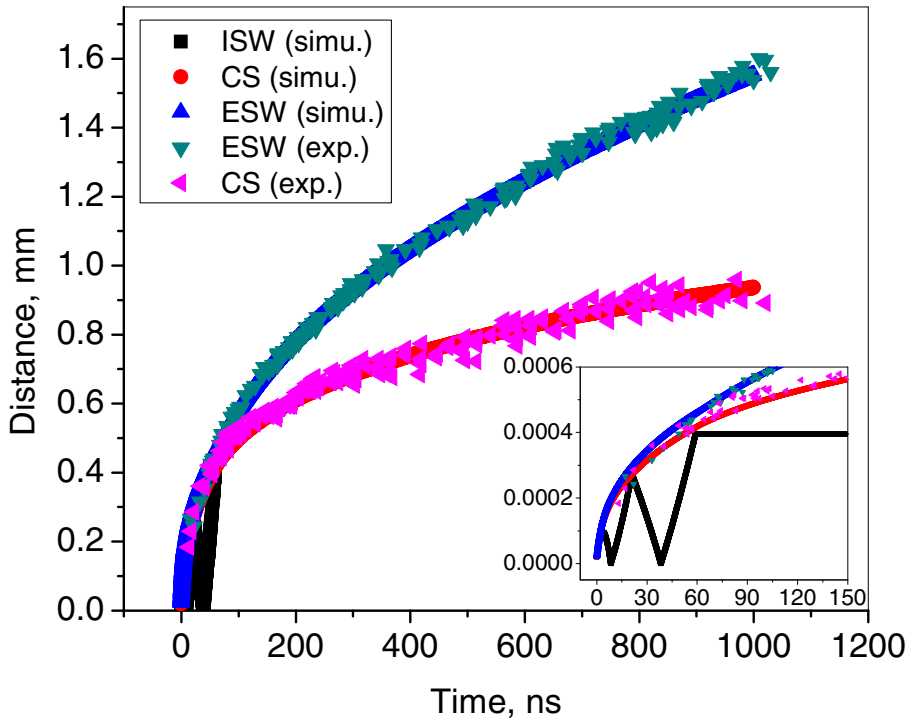

Figure 6

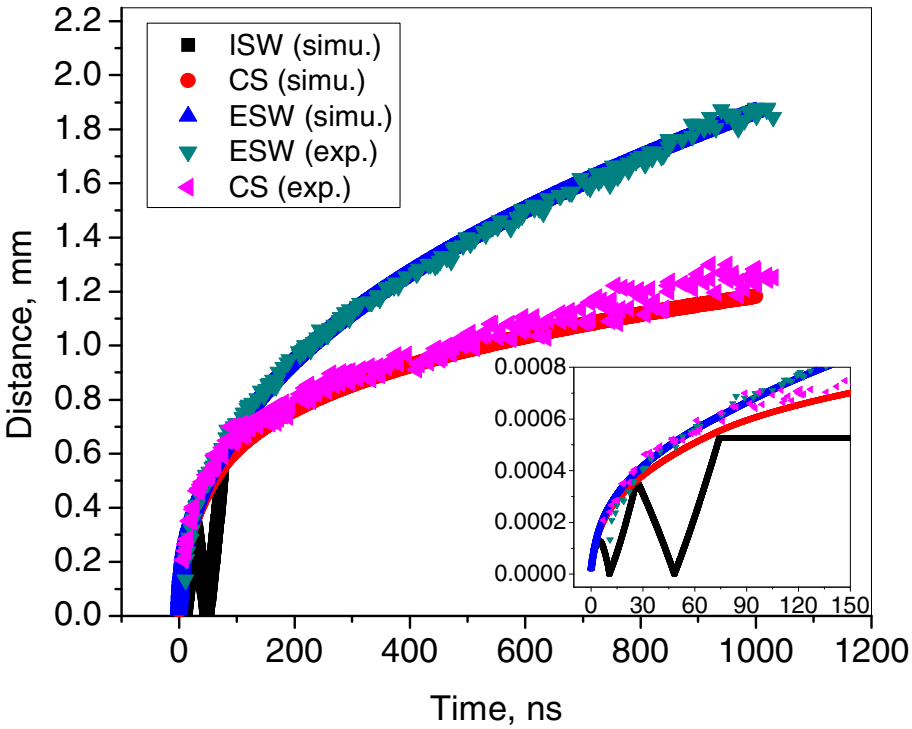

Figure 7

Laser ablation in Ar for E=10mJ (fluence $\approx 14 J/cm^2$)

	200 pulses	1 pulse	Simulation
Upper volume (μm^3)	140000	700	——
Down volume (μm^3)	170000	850	620
Net volume (μm^3)	-30000	-150	-620

Laser ablation in Ar for E=30mJ (fluence $\approx 42 J/cm^2$)

	200 pulses	1 pulse	Simulation
Upper volume (μm^3)	190000	950	——
Down volume (μm^3)	480000	2400	1460
Net volume (μm^3)	-290000	-1450	-1460

(a)

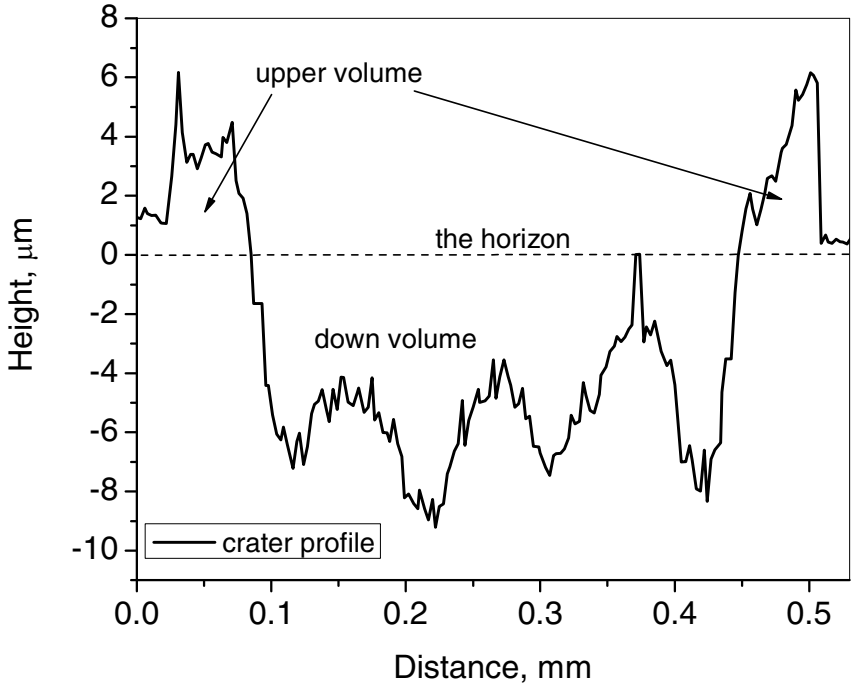

(b)

Figure 8

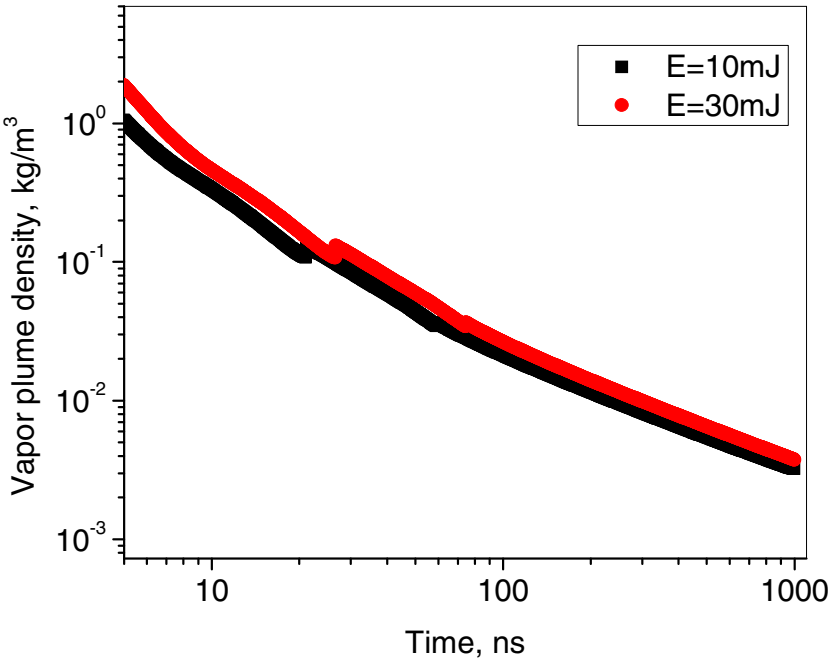

Figure 9.

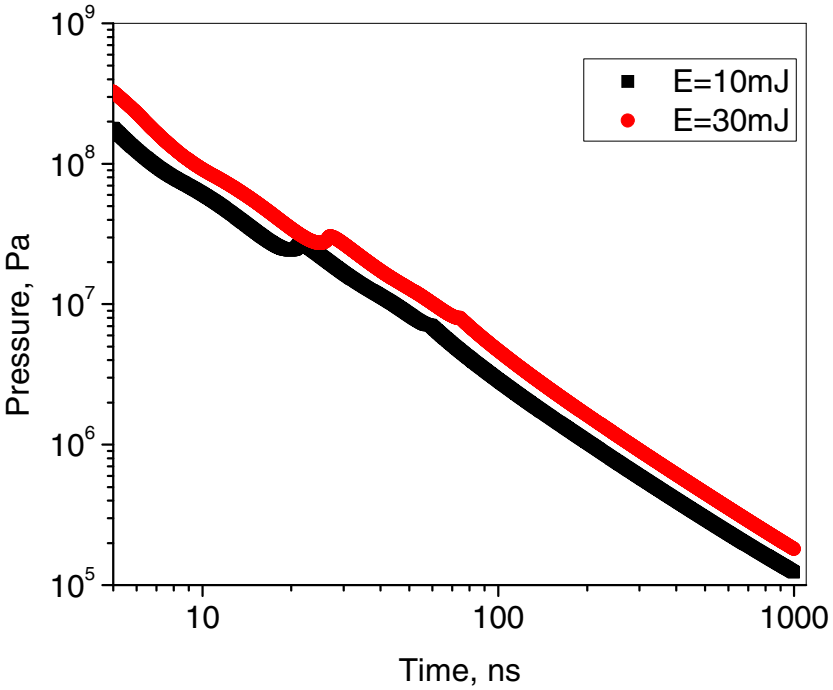

Figure 10.

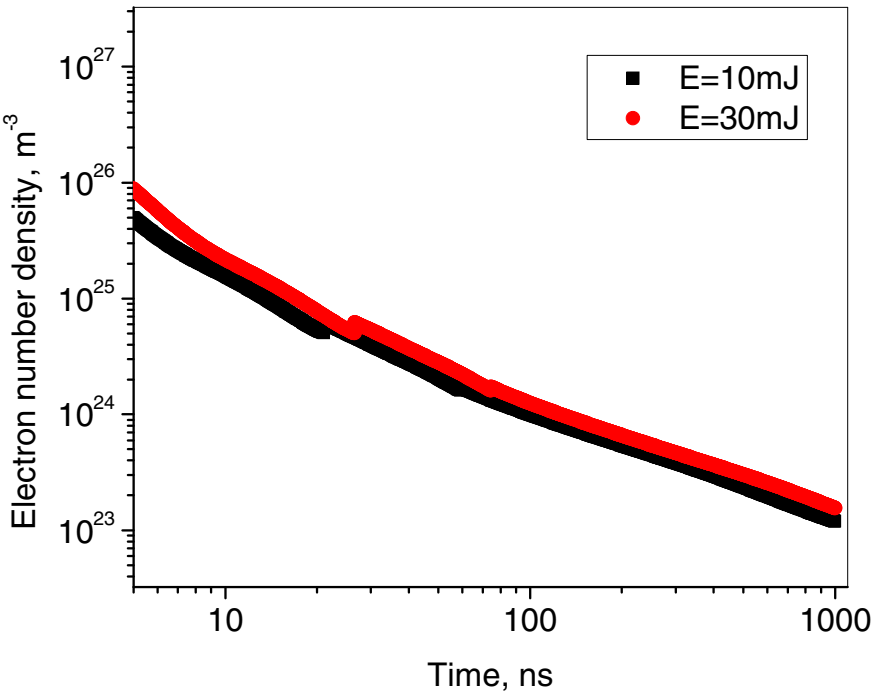

Figure 11.

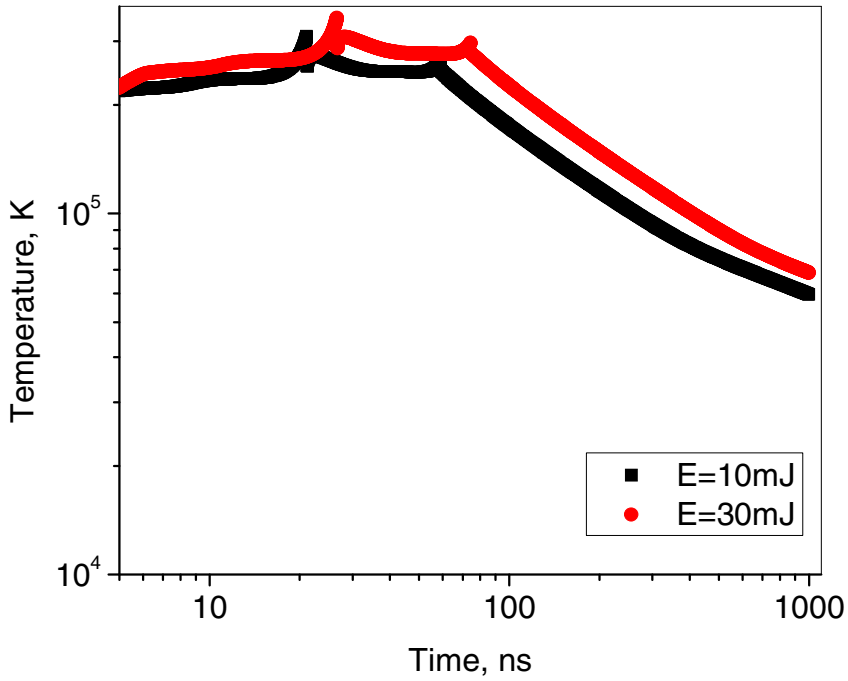

Figure 12.